Measurement of Biomimetic Deposition of Calcium Phosphate in Real Time Using Complex Capacitance

Alexander P. M. Guttenplan, Seppe Bormans, Zeinab Tahmasebi Birgani, Matthias Schumacher, Stefan Giselbrecht, Roman K. Truckenmüller, Pamela Habibović,* and Ronald Thoelen*

Deposition of minerals, particularly calcium phosphates such as hydroxyapatite, is an important process in the formation of hard tissues such as bone. Herein, a new, affordable, straightforward and nondestructive method based on complex capacitance spectroscopy, an application of electrochemical impedance spectroscopy, is described which allows repeated and real-time measurements of the same sample throughout the calcium phosphate deposition process. In contrast with end-point assays which require large numbers of samples to obtain useful time-course data, this method allows the kinetics of deposition to be measured using a single sample by measuring the impedance of a pair of interdigitated electrodes at a range of frequencies as the layer of mineral is deposited. Changes in the complex capacitance curve over time with deposition can be compared with images of the coating deposited on model substrates, and show different behavior depending on the composition of the coating and the conditions of deposition.

1. Introduction

Biomineralization is a process used by many organisms to integrate a mineral entity in an organic setting.[1] The deposition of calcium phosphate (CaP) on a collagenous matrix to form bone, which acts both as a remarkably strong supporting structure for other tissues and organs and as a reservoir for physiologically important ions, takes place under physiological conditions, and is sufficiently controlled that the skeleton maintains its integrity while ectopic mineralization is avoided.[2] Once formed, bone mineral is in a constant state of turnover. In healthy adult humans, ≈10% of bone mineral by mass is replaced each year, with resorption of existing bone mineral and deposition of new mineral in a fine balance to maintain constant bone mass.[3,4] The process of biomineralization is also used as an inspiration for the design of synthetic bone graft substitutes used for regeneration of large bone defects.[5] The potential of such biomaterials to aid in bone regeneration is often characterized in terms of their bone bioactivity, which can be correlated with the ability of apatite to form on their surface in a supersaturated CaP solution such as simulated body fluid (SBF).[6] For these reasons, a wide range of in vitro and ex vivo methods, on a variety of scales including microfluidic chips, have been developed to model the process of mineralization both in bone and in other hard tissues such as teeth and shells.[7]

Currently, most of the methods available to study (bio)mineralization involve end-point assays, often coupled to microscopic imaging. Mineralization can be measured by optical microscopy either by using a staining-based assay such as alizarin red[8] or by without staining using stereomicroscopy.[9] Cryoelectron microscopy has also been used to study the initial stages of bone mineralization.[10] In contrast to these end-point methods, in situ liquid-phase transmission electron microscopy[11] and quartz crystal microbalance[12] or surface acoustic wave[13] sensors have been used to study mineralization in real time, but have disadvantages including complexity and the need for expensive equipment.

Electrochemical impedance spectroscopy (EIS) is an established technique to investigate the electrical properties of materials.[14] An EIS measurement involves measuring the complex impedance at a range of frequencies. The data obtained can be displayed in a variety of ways, including a Nyquist plot (real

Dr. A. P. M. Guttenplan, Dr. Z. Tahmasebi Birgani, Dr. M. Schumacher, Dr. S. Giselbrecht, Prof. R. K. Truckenmüller, Prof. P. Habibović
Department of Instructive Biomaterials Engineering
MERLN Institute for Technology-Inspired Regenerative Medicine
Maastricht University
Universiteitssingel 40, Maastricht 6229ER, The Netherlands
E-mail: p.habibovic@maastrichtuniversity.nl

S. Bormans, Prof. R. Thoelen
Institute for Materials Research IMO
Hasselt University
Wetenschapspark 1, Diepenbeek B-3590, Belgium
E-mail: ronald.thoelen@uhasselt.be

S. Bormans, Prof. R. Thoelen
IMOMEC Division
IMEC vzw
Wetenschapspark 1, Diepenbeek B-3590, Belgium

(iD) The ORCID identification number(s) for the author(s) of this article can be found under https://doi.org/10.1002/pssa.202000672.

against imaginary impedance) or a Bode plot (magnitude and phase of impedance against frequency).[15] EIS has a wide range of applications outside biology and biomedicine, for example, monitoring the integrity of paint[16] or the deposition (scaling) of minerals on metal surfaces in industrial water systems.[17] Within biology, EIS is gaining popularity as a label-free real-time sensing technique, particularly for monitoring of epithelial barrier tissues.[18] Cell growth,[19] cell death,[20] and the changing properties of layers of cells as they differentiate, for instance, toward an osteogenic lineage,[21,22] have also been monitored using EIS.

The field of tissue engineering and regenerative medicine is a particularly interesting application for EIS, which could be used both to evaluate candidate biomaterials while reducing the use of animal models[23] and to evaluate the progress of regeneration. EIS-based methods have been used to follow the rate of implant osseointegration and fracture healing in vivo in animal models.[24] Fracture healing has been monitored using both external electrodes[25] and microelectrodes surgically implanted as part of bone plates at the fracture site.[26]

However, the translation of EIS studies of bone formation in vivo to the microfluidic environment, with its attendant advantages in terms of reduced reagent volume and the potential for high-throughput and automated studies,[27] remains relatively limited, in part because "bone on chip" models are a relatively immature field in comparison with microfluidic models of other tissues and organs.[28]

Investigations of the deposition of mineral on chip under biomimetic conditions using impedance have so far been limited to measurements at a single frequency and a single timepoint.[29] These measurements do not take full advantage of the benefits of EIS, both in terms of the potential to perform automated time-series measurements due to the noninvasive nature of the technique and in terms of the amount of information that can be obtained from a single measurement by performing a frequency sweep.

The data obtained from an EIS measurement can be interpreted in a number of ways. In most studies in the literature, only resistive behavior is visualized by analyzing changes in the real part or the modulus of the complex impedance. While changes in the phase of the complex impedance are also sometimes analyzed, this analysis is often relatively limited and qualitative. Next, equivalent circuit modeling is also used in which the material and/or interface under investigation is modeled as a set of electrical components such as resistances, capacitances, and impedances.[30] An alternative method of interest for the investigation of dielectric layers is capacitance spectroscopy, in which the complex impedance as a function of frequency $Z^*(\omega)$ is converted into a complex capacitance $C^*(\omega)$, itself a function of frequency, by $C^*(\omega) = 1/j\omega Z^*(\omega)$.[31] This method is particularly useful for the investigation of insulating coatings such as biologically relevant mineral layers, in which the coating acts as the dielectric of a capacitor.[32]

In this study, two different supersaturated CaP solutions—solution A, based on the composition of SBF but with increased concentration, which is known to deposit amorphous CaP (ACP) at physiological temperatures, and solution B, a similar solution with a higher concentration of CaP and a lower concentration of crystallization inhibitors, which deposits a biomimetic crystalline hydroxyapatite (HAP)—were used to deposit CaP on interdigitated electrodes (IDEs) over a timescale of 3 days at two different

temperatures. During deposition, the complex impedance of the electrodes was measured automatically at regular intervals. Model substrates consisting of the same materials as the IDEs, namely, gold and polyethylene terephthalate (PET), were also coated under the same conditions. The mineral coatings on these model substrates were characterized by confocal laser scanning profilometry, scanning electron microscopy (SEM), Fourier transform infrared (FTIR) spectroscopy, and X-ray diffraction (XRD). An increase in the complex capacitance over time as the coating formed was observed, and different kinetic behavior was exhibited both by different coating solutions and by the same solutions at different temperatures.

2. Results and Discussion

2.1. Phase Identification

CaP was deposited on IDEs in a well plate using two different solutions and at two different temperatures. To identify the composition of the deposited CaP layers, XRD patterns and FTIR spectra of the formed coatings after 72 h of deposition were collected (see **Figure 1** and **2**, Supporting Information). The results confirmed that two different forms of CaP were deposited, namely, an ACP and a crystalline HAP. Coating deposition using solution A at 37 °C gave the expected broad peak for an ACP phase with small peaks corresponding to brushite and beta calcium pyrophosphate. Deposition at 50 °C with both coating solutions gave an HA layer, though the coating deposited using solution A, which yielded ACP at 37 °C, appeared to be significantly less crystalline. For the material deposited using solution B, an increased crystallinity and crystallite size was determined for the samples deposited at 50 °C compared with those deposited at 37 °C (see Table S1, Supporting Information), which is in accordance with previous studies describing a steady increase in crystallite size with temperature.[33] FTIR spectra of coatings deposited from both solutions at both temperatures showed peaks corresponding to phosphate and carbonate groups (see Table S2, Supporting Information). Due to the relatively small amount of CaP deposited by solution A, the FTIR spectra of coatings formed with this solution also showed peaks corresponding to contamination by PET from the substrate which was scraped off for analysis along with the coating.

In addition to these measurements of the phase and crystallinity of the deposited material, electron microscopy and laser profilometry were used to give an indication of the morphology and homogeneity of the coating.

2.2. Coating Morphology

Figure 1 shows the SEM images of the coatings deposited under different conditions. Images were captured after 24 and 65 h of deposition as shown in the figure. These images show a clear difference between the layers deposited using the two solutions. The coating deposited using solution A at 37 °C appeared thin and amorphous after 24 h. Moreover, the surface was not homogeneously covered by the coating. After 65 h, the coating was thicker, contained some globular, semicrystalline deposits as well as amorphous material, and covered the surface more
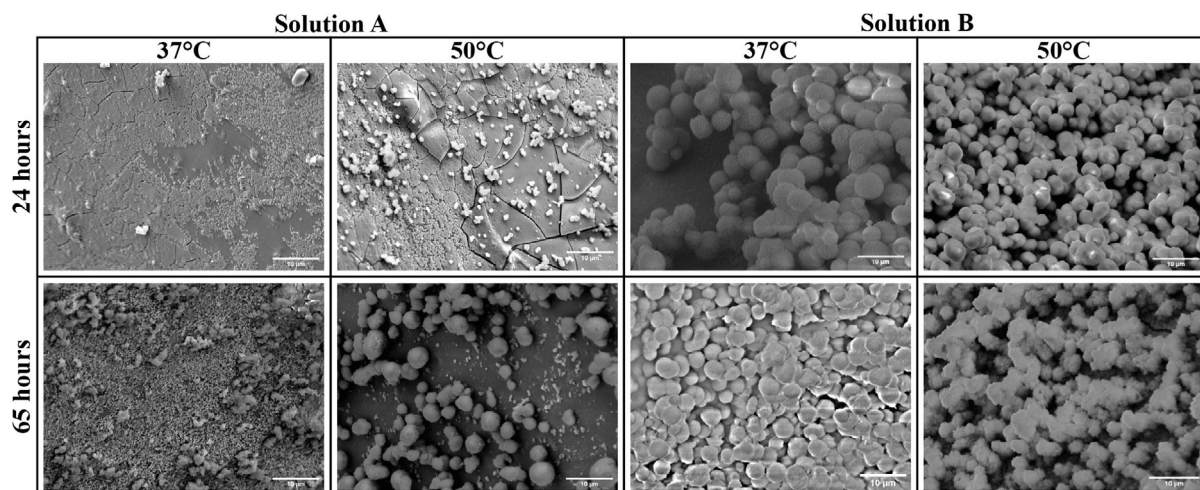
Figure 1. SEM images of the coatings deposited by the two different solutions at 37 and 50 °C after 24 and 65 h. [Scalebar = 10 μm].
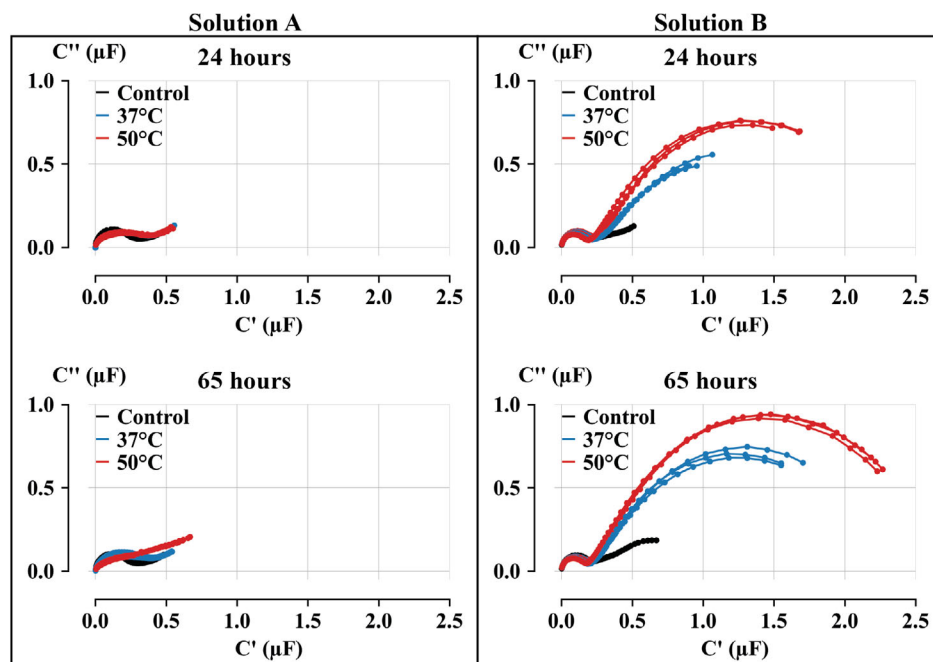
Figure 2. Complex capacitance Nyquist plots of the CaP coatings deposited using both solutions at 24 and 65 h.

homogeneously. At 50 °C, an amorphous layer and some poorly crystalline deposits were observed after 24 h, while after 65 h the nodules of these poorly crystalline deposits appeared larger. In contrast, the coatings deposited from solution B exhibited a globular crystalline structure, irrespective of the temperature. The coating deposited at 50 °C fully covered the surface after 24 h, while the coating deposited at 37 °C was less homogeneous. After 65 h, the homogeneity of the coatings deposited at both temperatures was high. These findings with respect to the morphology and homogeneity of the CaP coatings were supported by confocal laser scanning profilometry images (see Figure S3, Supporting Information).

2.3. EIS

Electrical properties of CaP layers are highly influenced by the hydroxide (OH^-) ions that are oriented along the c-axis at the center of the HA crystal lattice. In addition, it has been highlighted that the surface of HA is ionic in nature, which binds polar molecules such as water.[34] These water molecules give rise to proton-mediated conduction at low temperatures.

Therefore, in this article we choose to use EIS to monitor the change in the electrical properties of the CaP layer as it forms and becomes thicker. The impedance spectra were measured during the deposition of the CaP coatings under different conditions,

and complex capacitance Nyquist plots were created (Figure 2) for the coatings deposited by both solutions after 24 and 65 h of deposition.

The plots indicate a clear difference in the complex capacitance of the HAP layer deposited using solution B at both 37 and 50 °C, after both 24 and 65 h, compared with the control electrodes without deposition. The difference between the control electrodes and the layer deposited using solution A is only visible for deposition at 50 °C, where this solution also deposited a semicrystalline HAP layer. As the HAP layers are deposited over time, a thicker layer is formed, resulting in a further increase in the complex capacitance. The Nyquist complex capacitance plots show two circles: a smaller semicircle, corresponding to ohmic behavior at high frequency which remains constant over time and a larger semicircle corresponding to faradaic behavior at low frequency whose size increases over time.

As is described in greater detail in Section 4, this increase in the size of the second, low-frequency semicircle is directly related to an increasing double-layer capacitance. The increase in double-layer capacitance was less pronounced for deposition at 37 °C. The behavior of the complex capacitance plots correlates with the SEM images above where a fully formed layer of HA can be seen on the samples coated using solution B, while in solution A at 50 °C only some semicrystalline deposits were observed.

From the presence of the two semicircles in the complex capacitance spectra shown in Figure 2, it can be seen that two time constants are present at all conditions. These can be divided into two distinct frequency regions: first, the time constant in the high-frequency region, which remains constant and arises from the uncompensated ohmic resistance due to the electrolytic solution and the impedance characteristics resulting from the penetration of the electrolyte into the interstices between the globular CaP deposits, and second, the time constant in the low-frequency region, which varies with deposition and arises from processes taking place at the substrate–electrolyte interface.[35] Such behavior is typical for a metallic material covered by a porous film which is exposed to an electrolytic environment.[36]

Changes due to the formation of the CaP layer can therefore be observed in this second, low-frequency semicircle of the complex capacitance plot. These changes at the lower frequency range are also visible in the complex capacitance Bode plots which were plotted for the CaP layer deposited by solution B in **Figure 3**.

More specifically, the change in C'' with frequency in Figure 3 shows a clear change in the relaxation frequency, f_p, at which the maximum value of C'' is observed as the layer is formed. This frequency provides the dielectric relaxation time constant ($\tau_0 = 1/f_p$) for the whole system.[37] Nearly half of the low-frequency capacitance for the whole system is attained at τ_0. It can be seen that this relaxation frequency shifts to the right over time as the layer is formed. This higher f_p value and thus decreasing relaxation time constant are probably due to a decrease in the pseudocapacitance. This pseudocapacitance is the manifestation of redox effects happening at the CaP interface. A thicker layer of CaP acts as the blocking contact, which prevents charge-transfer reactions in a physiological solution.[31,38]

The imaginary part of the complex capacitance also increases over time. As the peak area relates to the total capacitance and C_{dl} increases as the layer grows, the total capacitance will increase, resulting in an increase in C''. The increase in C_{dl} can be attributed to the increase in surface area due to deeper pores.[35] This figure also shows a clear change in the real part of the complex capacitance during the deposition at both 37 and 50 °C. To investigate the dynamics of the deposition process, the real part of the complex capacitance, C', in the lower frequency regime can be plotted over time.
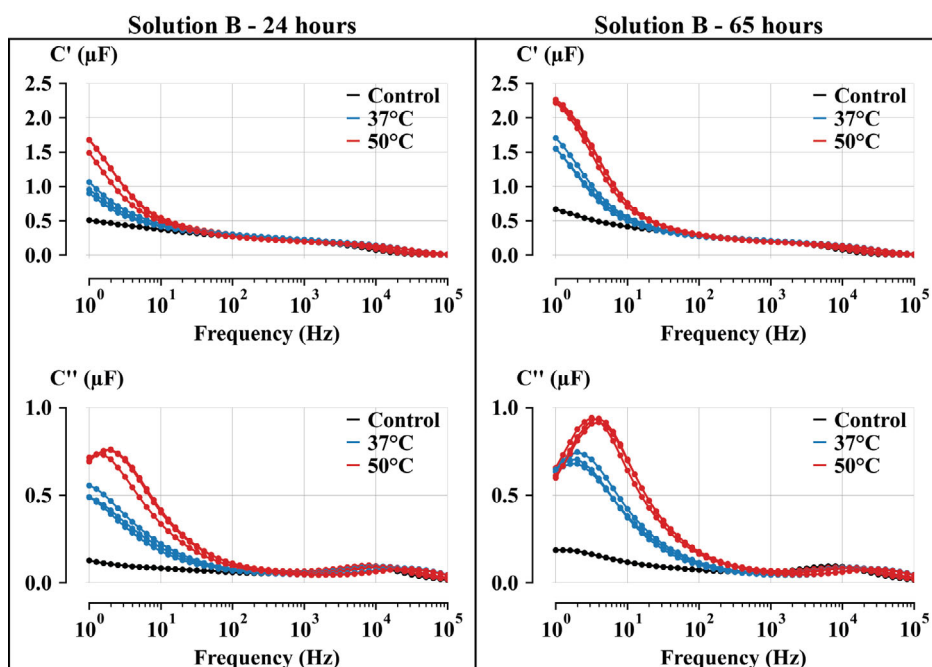
Figure 3. Complex capacitance Bode diagrams of the CaP coatings deposited using solution B.

ADVANCED
SCIENCE NEWS
www.advancedsciencenews.com

physica
status solidi a
www.pss-a.com
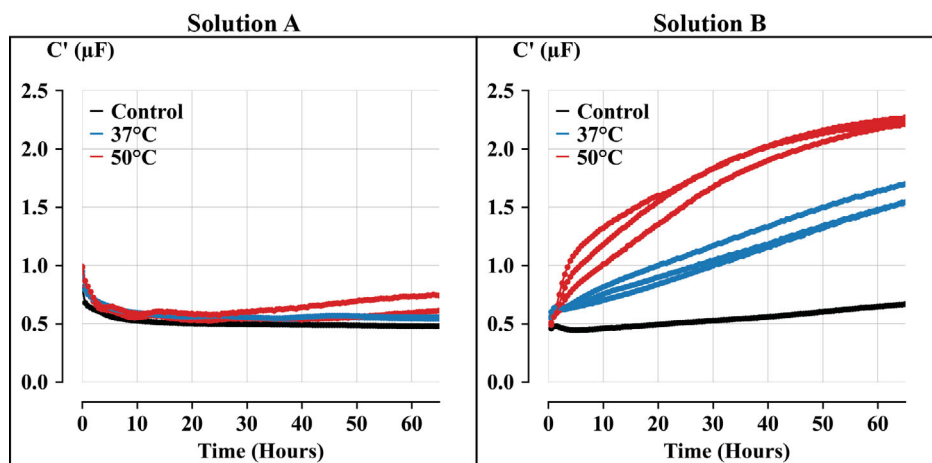
Figure 4. Change in real part of complex capacitance C' at a frequency of 1 Hz over time.

In **Figure 4**, this dynamic behavior of the growth process is clearly visible. Compared with the reference electrode without coating, signals from the electrodes coated using solution B at both 37 and 50 °C increase over time. The increase in C' for the electrodes coated at 37 °C is less pronounced than that for the electrodes coated at 50 °C. A steep increase in C' can be observed for the first 3 h of deposition using solution B at 50 °C. This steep increase compared with the latter parts of the growth process is less pronounced for the measurements performed at 37 °C. The change in the real part of the complex capacitance, C', for the layers deposited using solution A is far less pronounced. An increase in C' is only observed at 50 °C.

The value of the real part of the capacitance at these low frequencies is a measure of capacitance stored in the system. For porous layers such as these, it is an indication of the amount of electrolyte ions which can access the pores deep inside the material. For the complete HAP layers deposited by solution B at 50 °C, the porosity appeared to be higher, resulting in a higher absolute real part of the capacitance value.[39] These findings are also visualized in the frequency spectra of Figure 3, in which the layers deposited using solution B exhibit a noticeable increase in their real capacitance at lower frequencies, which can be explained by electrolyte ions penetrating the pores of the deposited layers. At higher frequencies, the electrolyte ions can only access the surface of the porous material, due to the time required for them to migrate into the pores.[40,41] Therefore, the capacitance at these frequencies is mainly related to the electrolyte concentration in the bulk liquid. These differences in capacitance are not present for the layers deposited using solution A, where there is no clear porous layer present.

3. Conclusion

In this article, the deposition of CaP using two different biomimetic solutions at two different temperatures was analyzed. The study showed that solution B deposited a crystalline HAP layer at both temperatures, while solution A led to the deposition of a predominantly amorphous layer, with some semicrystalline deposits when the deposition was performed at 50 °C. The

SEM studies showed that the HA layer deposited by solution B was homogeneous and consisted of globular crystalline deposits, while the layer deposited by solution A was less homogeneous and consisted largely of amorphous material. These findings, which are in agreement with literature, were confirmed by laser profilometry, FTIR spectroscopy, and XRD.

To monitor the deposition in real time, the complex capacitance parameters were monitored. This electrochemical analysis revealed that several physical parameters were influenced by the different deposition conditions. The Nyquist and Bode plots of complex capacitance show that the largest influence of the insulating CaP layers occurred in the lower frequency regime. The physical parameters of the porous layers which were formed under different conditions influenced the interaction of the ions with the electrodes. The specific interaction of the ions with the HA layer deposited from solution B was obvious from the changes in the imaginary part of the complex capacitance. The changes in the real part of the complex capacitance showed that this value is significantly influenced by the amount of ions in the porous layer, which increases with the thickness of the layer, resulting in the ideal parameter to investigate the dynamic behavior of deposition.

The method presented in this proof of concept study will allow the deposition process of mineral layers to be more closely monitored as a function of time. The deposition of mineral layers on biologically relevant substrates, or in the presence of cells, could be studied in future using this technique. This is of great interest in the research field of biomineralization as well as regenerative medicine, where the physical and chemical interaction of adherent cells with CaP layers can be studied using this same analysis technique. Currently, this method is limited to the study of mineralization on flat 2D substrates, which do not resemble the microenvironment of biomineralization in vivo. This difference is of particular importance given the role of substrate microstructure in biomineralization and osteoinduction.[42] In future, 3D or microstructured substrates could be fabricated containing interdigitated micro- or nanoelectrodes to investigate the effect of local microstructure differences on the kinetics of CaP deposition.

2000672 (5 of 8)

4. Experimental Section

Unless otherwise stated, all chemicals were obtained from commercial suppliers in reagent or higher grade and used as received without further purification.

Calcium Phosphate Deposition: Coatings were deposited on the electrodes using a biomimetic precipitation method as previously described in the literature. Solution A, which deposits an ACP layer at 37 °C, was similar to Kokubo's SBF[43] but 2.5× more concentrated.[44] Solution B, which deposits a layer of HAP at 37 °C, was similar to solution A but with double the concentration of calcium and phosphate, no Tris buffer, and with a lower concentration of Mg^{2+} which inhibits crystal growth.[45] In all cases, the electrodes were rinsed with milliQ water to remove dust before 200 μL of the relevant coating solution was dispensed into each well of the well plate, and the plate incubated at either 37 or 50 °C while measuring the changes in electrical impedance as described earlier. Two wells were filled with Tris-buffered saline (50 mM Tris pH 7.4, 150 mM NaCl) as controls to compensate for any drift in the sensor readings during incubation.

To validate that the observed changes in impedance were due to the deposition of the coating and not to depletion of ions from the solution, a well was filled with Tris-buffered saline and the impedance spectrum measured before coating. The well was then rinsed with water and coated with CaP using solution A at 37 °C as described earlier, before the coating solution was removed and the well rinsed, refilled with Tris-buffered saline, and the impedance spectrum measured again. The same procedure was followed with a control well that was incubated in Tris-buffered saline during the coating period, which was replaced with fresh solution before the second measurement. As the solution in the well was identical before and after coating, the observed changes in the impedance were due to the presence of the coating (see Figure S4, Supporting Information).

Model Substrates: To characterize the coatings without expending IDEs, small token-type substrates were produced that replicated the e-Plate structure of gold electrodes on PET. Approximately 1×1 cm (for SEM and profilometry) or 4×4 cm (for XRD and FTIR) pieces of PET (Goodfellow, Hamburg, Germany; 500 μm thickness) were cut out and partially coated with gold (SC7620 sputter coater, Quorum Technologies, Laughton, UK; 15 s, 18 mA) using Scotch tape to mask off areas of bare PET. These model substrates were rinsed with milliQ water before being placed in Petri dishes and coated using the same precipitation process as the electrodes. The model substrates were used for all measurements other than EIS.

Characterization of Model Substrates: Coated substrates were imaged using a VK-X200 confocal laser scanning microscope (Keyence, Osaka, Japan) in surface profile mode. Substrates were also sputter-coated with gold and imaged using an XL-30 field emission scanning electron microscope (FEI, Eindhoven, The Netherlands) using 45° tilted stubs. To identify the chemical phase, the coating was manually removed from the substrate and characterized using FTIR spectroscopy and powder XRD. Attenuated total reflection (ATR) FTIR analysis was performed using a Nicolet iS50 spectrometer (Thermo, Breda, The Netherlands), running 32 scans between 400 and 4000 cm^{-1} with a resolution of 0.5 cm^{-1}. Material scraped off an uncoated substrate was used to collect a "blank" spectrum. Spectra were evaluated using version 1.2.10 of Spectragryph.[46] X-ray diffractograms were collected using a D2 Phaser diffractometer (Bruker, Leiderdorp, The Netherlands). Cu Kα radiation ($\lambda = 1.5406$ Å) was used. Samples were scanned in the range of $6° \leq 2\theta \leq 60°$ in increments of 0.02° with an integration time of 0.75 s. Diffraction data were analyzed using Profex.[47]

EIS: EIS measurements were performed using a PalmSens 4 electrochemical interface (PalmSens BV, Houten, The Netherlands), controlled by PSTrace 5.7 software. The impedance spectra were measured over a frequency range from 1 Hz to 100 kHz at ten frequencies per decade, with an AC voltage of 0.01 V and a current range of 1 nA to 10 mA. The total duration of the measurements was 72 h, with impedance spectra being measured automatically every 30 min. Using the MUX8-R2 multiplexer (PalmSens), changes in the impedance of up to eight different electrode pairs could be followed simultaneously. In this work, commercially available well plates (e-Plate 16 PET, Agilent, San Diego, CA, USA) designed for the xCELLigence Real-Time Cell Analyzer were used for the impedance measurements. These well plates each contain 16 wells with the same dimensions as those of a standard 96-well microtiter plate. The bottoms of these wells consist of PET on which interdigitated gold microelectrodes, covering ≈70–80% of the surface, are printed. The well plates were connected to the PalmSens electrochemical interface by means of a custom-fabricated printed circuit board (PCB) connector (see **Figure 5**).

Data Analysis: Plots of complex electrochemical impedance Z and complex capacitance C were utilized to support the frequency domain analysis of the electric double-layer capacitance of the calcium phosphate layer.[48] In this work, the complex capacitances were calculated using a transmission line model (TLM)[32] to model the electrochemical response of porous electrodes.[39] Using the real and imaginary parts, Z' and Z'', respectively, from the complex impedance data, the complex capacitance was calculated using the following equation
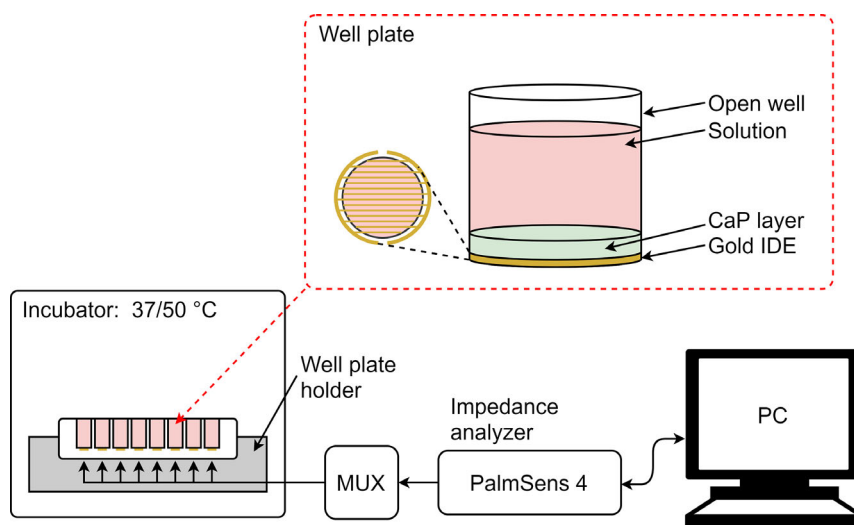
Figure 5. Schematic overview of the measurement setup. A PalmSens 4 electrochemical interface is connected to commercially available well plates to perform the measurements.
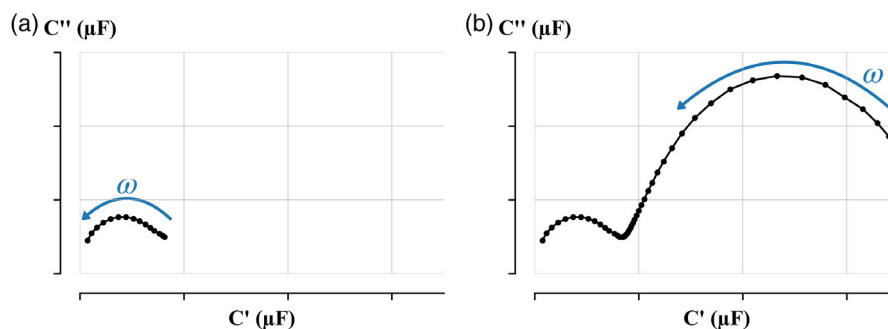
Figure 6. Schematic representation of the semicircles formed by the Nyquist plot of complex capacitance during growth of a CaP layer.
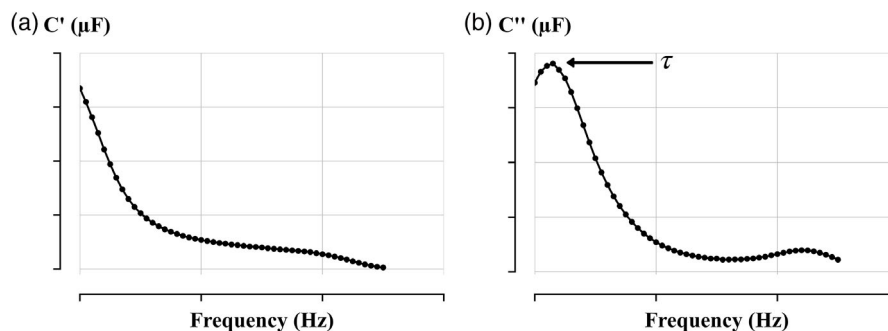
Figure 7. a) Real part of complex capacitance C' versus frequency and b) imaginary part of complex capacitance C'' versus frequency.

$$C' = -\frac{Z''}{\omega(Z'^2 + Z''^2)} \quad C'' = -\frac{Z'}{\omega(Z'^2 + Z''^2)} \quad (1)$$

In this case, the calculated complex capacitances represent the electric equivalent model of a series circuit of R_{sol} and C_{dl}. The resistance of the solution is represented by R_{sol}, while C_{dl} represents the capacitance double layer caused by the dielectric properties of the CaP film. The complex capacitance Nyquist plots describe the locus of a semicircle in the complex plane when plotting C' against C'', as shown in **Figure 6**.

Figure 6a represents the presence of one capacitive behavior, where the locus converges at the origin and C_{dl} in high and low frequency ranges, respectively. The time constant of the dielectric relaxation $R_{sol}C_{dl}$ can be obtained from the frequency f_0 where the imaginary part of the complex capacitance reaches its maximum value[35]

$$R_{sol}C_{dl} = \frac{1}{2\pi f_0} \quad (2)$$

Furthermore, the low-frequency limiting value of the capacitance is as follows

$$C'_{\omega \to 0} = C_{dl}$$
$$C''_{\omega \to 0} = 0 \quad (3)$$

When there are two capacitive behaviors present, the complex capacitance Nyquist plots will indicate two semicircles overlapping with each other, as shown in Figure 6b. The plots are thus used to analyze the presence of the capacitive behavior due to the CaP film. Next, to plot the capacitive behavior over time a frequency was chosen representing the C_{dl} of the CaP film. This results in time-based graphs of the CaP growth.

Figure 7a shows the variation of the real part of the capacitance with respect to frequency. The variation of the capacitance as a function of the frequency represents the electrolyte ion penetration inside the pores of the material. At lower frequencies, the electrolyte ions migrate deep

into the pores of the material and thus C' increases. However, at high frequencies, the electrolyte ions can only access the surface of the porous material and hence C' decreases. At very high frequencies, the material behaves like a resistor and C' becomes independent of the frequency. Figure 7b shows the change in imaginary part of the complex capacitance with frequency. The imaginary capacitance attains a maximum at a frequency f_0. The inverse of this frequency provides the dielectric relaxation time constant (τ_0) for the whole system. The evolution of τ_0 can also provide information about the growth properties of the CaP films. All data were analyzed, and the plots were generated, using an in-house EIS analysis platform.

Supporting Information

Supporting Information is available from the Wiley Online Library or from the author.

Acknowledgements

Conflict of Interest

The authors declare no conflict of interest.

[1] H. A. Lowenstam, S. Weiner, *On biomineralization*, Oxford University Press, New York **1989**.

[2] N. Reznikov, J. A. M. Steele, P. Fratzl, M. M. Stevens, *Nat. Rev. Mater.* **2016**, *1*, 16041.

[3] L. J. Raggatt, N. C. Partridge, *J. Biol. Chem.* **2010**, *285*, 25103.

[4] B. Clarke, *Clin. J. Am. Soc. Nephrol.: CJASN* **2008**, *3*, 131.

[5] D. de Melo Pereira, P. Habibovic, *Adv. Healthcare Mater.* **2018**, *7*, 1800700.

[6] T. Kokubo, H. Takadama, *Biomaterials* **2006**, *27*, 2907.

[7] V. Sharma, A. Srinivasan, F. Nikolajeff, S. Kumar, *Acta Biomater.* **2021**, *120*, 20.

[8] C. A. Gregory, W. G. Gunn, A. Peister, D. J. Prockop, *Anal. Biochem.* **2004**, *329*, 77.

[9] R. Osorio, I. Cabello, M. Toledano, *J. Dent.* **2014**, *42*, 403.

[10] F. Nudelman, K. Pieterse, A. George, P. H. Bomans, H. Friedrich, L. J. Brylka, P. A. Hilbers, G. de With, N. A. Sommerdijk, *Nat. Mater.* **2010**, *9*, 1004.

[11] X. Wang, J. Yang, C. M. Andrei, L. Soleymani, K. Grandfield, *Commun. Chem.* **2018**, *1*, 80.

[12] G. Conklin, S. C. Ngourn, A. E. Gerdon, *Sens. Actuators, B* **2015**, *214*, 174.

[13] A. Pohl, I. M. Weiss, *Beilstein J. Nanotechnol.* **2014**, *5*, 1823.

[14] M. Grossi, B. Riccò, *J. Sens. Sens. Syst.* **2017**, *6*, 303.

[15] E. P. Randviir, C. E. Banks, *Anal. Methods* **2013**, *5*, 1098.

[16] D. Loveday, P. Peterson, B. Rodgers, *J. Coat. Technol.* **2004**, *1*, 46.

[17] H. Li, D. Dzombak, R. Vidic, *Ind. Eng. Chem. Res.* **2012**, *51*, 2821.

[18] T. Gerasimenko, S. Nikulin, G. Zakharova, A. Poloznikov, V. Petrov, A. Baranova, A. Tonevitsky, *Front. Bioeng. Biotechnol.* **2020**, *7*, 474.

[19] G. H. Lee, J.-C. Pyun, S. Cho, *J. Nanosci. Nanotechnol.* **2014**, *14*, 8342.

[20] A. Mansoorifar, A. Koklu, A. Beskok, *Anal. Chem.* **2019**, *91*, 4140.

[21] C. Hildebrandt, H. Büth, S. Cho, H. Thielecke, *J. Biotechnol.* **2010**, *148*, 83.

[22] R. C. Nordberg, J. Zhang, E. H. Griffith, M. W. Frank, B. Starly, E. G. Loboa, *STEM CELLS Trans. Med.* **2017**, *6*, 502.

[23] M. Amini, J. Hisdal, H. Kalvøy, *J. Electr. Bioimpedance* **2018**, *9*, 142.

[24] M. T. Ehrensberger, C. M. Clark, M. K. Canty, E. P. McDermott, *Biomed. Eng. Lett.* **2020**, *10*, 17.

[25] E. Kozhevnikov, X. Hou, S. Qiao, Y. Zhao, C. Li, W. Tian, *J. Mater. Chem. B* **2016**, *4*, 2757.

[26] M. C. Lin, D. Hu, M. Marmor, S. T. Herfat, C. S. Bahney, M. M. Maharbiz, *Sci. Rep.* **2019**, *9*, 1.

[27] Š. Selimović, H. Kaji, H. Bae, A. Khademhosseini, *Microfluidic Cell Culture Systems*, Elsevier, Amsterdam/New York **2019**, pp. 31–63.

[28] A. Mansoorifar, R. Gordon, R. C. Bergan, L. E. Bertassoni, *Adv. Funct. Mater.* **2021**, *31*, 2006796.

[29] R. Ramos, K. Zhang, D. Quinn, S. W. Sawyer, S. Mcloughlin, P. Soman, *Bioelectricity* **2019**, *1*, 73.

[30] M. Moisel, M. A. F. L. De Mele, W. D. Müller, *Adv. Eng. Mater.* **2008**, *10*, 33.

[31] P. R. Bueno, G. Mizzon, J. J. Davis, *J. Phys. Chem. B* **2012**, *116*, 8822.

[32] M. Itagaki, S. Suzuki, I. Shitanda, K. Watanabe, *Electrochemistry* **2007**, *75*, 649.

[33] S. György, Z. Károly, P. Fazekas, P. Németh, E. Bódis, A. Menyhárd, L. Kótai, S. Klébert, *J. Therm. Anal. Calorim.* **2019**, *138*, 145.

[34] M. Nagai, T. Nishino, *Solid State Ionics* **1988**, *28–30*, 1456.

[35] J. H. Jang, S. M. Oh, *J. Electrochem. Soc.* **2004**, *151*, A571.

[36] A. Oz, S. Hershkovitz, N. Belman, E. Tal-Gutelmacher, Y. Tsur, *Solid State Ionics* **2016**, *288*, 311.

[37] J. H. Jang, S. Jeon, J. H. Cho, S.-K. Kim, S.-Y. Lee, E. Cho, H.-J. Kim, J. Han, T.-H. Lim, *J. Electrochem. Soc.* **2009**, *156*, B1293.

[38] J. Katić, M. Metikoš-Huković, R. Babić, *J. Appl. Electrochem.* **2014**, *44*, 87.

[39] M. Arunkumar, A. Paul, *ACS Omega* **2017**, *2*, 8039.

[40] M. Kim, I. Oh, J. Kim, *Phys. Chem. Chem. Phys.* **2015**, *17*, 16367.

[41] M. Biswal, A. Banerjee, M. Deo, S. Ogale, *Energy Environ. Sci.* **2013**, *6*, 1249.

[42] M. Bohner, R. J. Miron, *Mater. Today* **2019**, *22*, 132.

[43] T. Kokubo, H. M. Kim, M. Kawashita, *Biomaterials* **2003**, *24*, 2161.

[44] S. Patntirapong, P. Habibovic, P. V. Hauschka, *Biomaterials* **2009**, *30*, 548.

[45] P. Habibovic, F. Barrère, C. A. van Blitterswijk, K. de Groot, P. Layrolle, *J. Am. Ceram. Soc.* **2002**, *85*, 517.

[46] F. Menges, Spectragryph- Optical Spectroscopy Software, http://www.effemm2.de/spectragryph (accessed: February 2019).

[47] N. Doebelin, R. Kleeberg, *J. Appl. Crystallogr.* **2015**, *48*, 1573.

[48] J.-H. Jang, S.-M. Oh, *J. Korean Electrochem. Soc.* **2010**, *13*, 223.